State-of-Health Estimation for Lithium-Ion Batteries Based on Decoupled Dynamic Characteristic of Constant-Voltage Charging Current

Jufeng Yang, *Member, IEEE*, Yingfeng Cai, *Senior Member, IEEE*, and Chunting Chris Mi, *Fellow, IEEE*

***Abstract*— State-of-health (SoH) is one of the critical battery states that must be estimated and closely monitored by the on-board battery management system in electric vehicles (EVs). In this study, the battery SoH, especially the capacity fade, is calculated based on the decoupled characteristic of the charging current under the constant-voltage (CV) scenario. First, a dynamic-decoupled parameter identification method is proposed to extract the parameters of the simplified second-order resistor–inductor (*RL*) network-based equivalent circuit model (ECM), developed by the authors. Second, the dynamic characteristics of the decoupled CV charging currents at different aging states are qualitatively investigated, and the corresponding time constant is selected as a feature-of-interest (FoI) to reflect the battery capacity degradation. Third, the aging data based on two types of lithium-ion batteries are employed to evaluate the performance of the proposed method. Verification results demonstrate that the proposed parameter identification method yields a reduced computational cost with a satisfactory fitting performance, compared to the conventional methods. The proposed parameterization method and the selected FoI guarantee the root-mean-square errors of the estimated SoH less than 2%, and the comparative results further validate the superiority of the selected FoI in terms of the SoH estimation accuracy.**

***Index Terms*— Constant-voltage (CV) charge, feature-of-interest (FoI), lithium-ion battery, parameter identification, state-of-health (SoH).**

I. INTRODUCTION

ELECTRIC vehicles (EVs) have become more and more popular in the past decade due to their superior performance, ability to displace fossil fuel, and reduction in greenhouse gas emissions [1]. The onboard energy storage systems, namely lithium-ion batteries, are considered as the crucial component in EVs. The driving range, charging time, life cycle, and safety are major concerns of the onboard energy storage system [2], [3]. In particular, the state-of-health (SoH) of the onboard battery is an essential parameter that should be accurately estimated and monitored to ensure a safe and reliable operation [4], [5]. In general, the actual battery capacity is one of the critical battery health indicators as it degrades over time with cycle usage. Considerable research efforts have been conducted recently to estimate the actual battery capacity.

A. Problem Statement

The actual battery capacity can be directly measured through test-based methods. However, these kinds of method require extensive test effort as well as expensive test equipment, which is unavailable for on-board applications [6]. Hence, the research on the SoH estimation is mainly focused on directly identifying the actual battery capacity or extracting the feature-of-interest (FoI) to characterize the actual battery capacity, based on the battery operating data. Compared to the discharging scenario, the data in the charging scenario are relatively stable, predictable, and rich in aging information. The existing charging protocols include constant-current constant-voltage (CC–CV), CC–CV–CC, constant-power CV (CP–CV), multistage-constant-current CV (MC-CCV), and so on [7]–[9], as shown in Fig. 1, where V_{cut} and V_{tr} represent the charge cutoff voltage and the transition voltage, respectively, and $V_{\mathrm{cut}} \geq V_{\mathrm{tr}}$. It can be seen that CC and/or CV phases are widely utilized in the charging protocols. Therefore, the charging data-based SoH estimation methods can be further divided into the CC charging data-based and the CV charging data-based methods in terms of the utilized data.

B. Related Works

For the CC charging data, the incremental capacity (IC) and the differential voltage (DV) analyses are two widely used techniques [10]–[12]. These two techniques transform the plateau regions in the voltage curve into the identifiable peaks/valleys in the IC/DV curves by differentiating the capacity/voltage with respect to the voltage/capacity. The aging-sensitive peak/valley information, such as corresponding location, magnitude, width, and area, is extracted as the FoI to correlate with the battery capacity loss. It should be noted that this kind of technique is sensitive to the previous discharging process, that is, the initial charging point [13], [14]. The SoH estimation performance may deteriorate when the battery is charged from the nonzero state-of-charge (SoC).

Manuscript received July 27, 2021; revised October 7, 2021; accepted October 27, 2021. Date of publication November 8, 2021; date of current version April 20, 2022. This work was supported in part by the National Science Foundation, USA, under Grant 1507198, in part by the China Postdoctoral Science Foundation under Grant 2020M671356, in part by the Natural Science Foundation of Jiangsu Province under Grant BK20210773, and in part by the National Natural Science Foundation of China under Grant U1764257. *(Corresponding authors: Chunting Chris Mi; Yingfeng Cai.)*

Jufeng Yang and Yingfeng Cai are with the Automotive Engineering Research Institute, Jiangsu University, Zhenjiang 212013, China (e-mail: yjf@ujs.edu.cn; caicaixiao0304@126.com).

Chunting Chris Mi is with the Department of Electrical and Computer Engineering, San Diego State University, San Diego, CA 92182 USA (e-mail: mi@ieee.org).

Digital Object Identifier 10.1109/TTE.2021.3125932

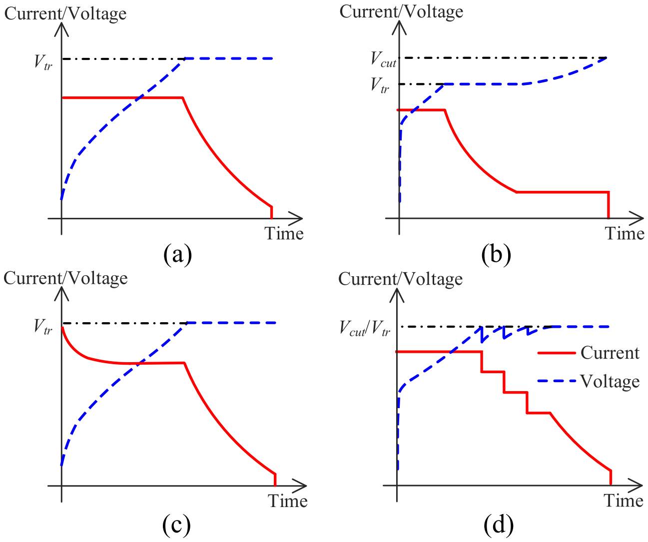

Fig. 1. Schematic representation of different charging protocols. (a) CC–CV. (b) CC–CV–CC. (c) CP–CV. (d) MC-CCV.

Besides the CC phase, the existing research has revealed that the electrochemical reactions occurring during the CV phase also demonstrate a remarkable influence on the battery SoH [15]–[17]. In addition, since the CV phase begins when the battery terminal voltage reaches the predetermined V_{tr}, as shown in Fig. 1, the CV phase is more robust to the uncertain initial charging state in comparison to the CC phase. Extensive studies have been conducted to extract the FoI from the CV charging data to reflect the actual battery capacity. For example, the CV charging time (T_{CV}) is found to increase monotonically with respect to the degrading capacity and is considered as an effective FoI in the literature to determine the battery SoH [18], [19]. Furthermore, the CV–CC time ratio was proposed in [20] as an FoI for the qualitative degradation analysis. The relative energy [21], the current interval, and the charging capacity [22] measured at CV phase were also considered as effective FoIs for aging investigation and SoH estimation. Besides, the kinetic behavior of the CV charging current is also useful for the battery SoH estimation. Specifically, constructing an accurate and efficient model, as well as selecting the aging-sensitive model parameters are two critical aspects to extract the FoI from the CV charging current curve. In [21], a simple exponential-based empirical function was employed to simulate the charging current under the CV scenario, and a linear correlation between the capacity loss and one function coefficient was discovered to represent the battery SoH. Similarly, Wang *et al.* [23] employed the *RC* network-based equivalent circuit model (ECM) to characterize the CV charging current and selected one model parameter to indicate the battery capacity degradation. In our previous work, the expression of the current time constant was derived based on the conventional ECM and was correlated with the normalized battery capacity [24]. Dingari *et al.* [25] developed a reduced-order electrochemical model to describe the evolution of current under the CV charging scenario and further proposed a coupled SoC and SoH estimation method based on the CC–CV charging data.

It should be noted that the model parameters in the above literature are mostly determined by the nonlinear least-squares (NLS) method. The NLS method starts at the predetermined initial values and searches the model parameters to best fit the estimated current to the measured values. One of the limitations of this kind of method lies in the fact that the identified parameters are sensitive to the predetermined initial and boundary conditions [26], [27]. If inappropriate initial and/or boundary values are selected, there is a high possibility that the cost function will converge to the local minimum. Furthermore, this method is computationally extensive, especially when the initial values are far from the optimal values [28], [29]. By contrast, the analytical method is relatively simple and has been utilized to identify the *RC* network parameters in the conventional ECM. Based on the voltage relaxation characteristics, Hentunen *et al.* [28] directly calculated the *RC* elements using the measured data in predefined windows. Furthermore, the relaxation dataset was split into the logarithmic subsets in [27], and only one *RC* element was fit based on each subset, with the initial values that were analytically derived from the voltage signal.

In order to accurately characterize the CV charging current, a resistor–inductor (*RL*) network-based ECM was proposed in our previous work, and the simplified second-order model was further developed to reduce the parameterization effort [30]. With the simplified second-order model, this article develops an online SoH estimation method based on the decoupled dynamics of the CV charging current. The main contributions of this article are: 1) a parameter identification method is proposed based on the decoupled dynamic characteristics of the CV charging current; 2) the time constant of the decoupled CV charging current is selected to correlate with the actual battery capacity; and 3) two battery degradation datasets based on batteries with different electrode materials are adopted to validate the effectiveness and the generality of the proposed method.

II. Proposed Parameter Identification Method

In our previous work, an *RL* network-based ECM was developed to characterize the dynamic behavior of the CV charging current, and a model containing two parallel-connected *RL* networks was found to be a preferred choice, considering both the model accuracy and the parameterization effort. In this study, this second-order *RL* network-based ECM is employed as the basis for the battery SoH estimation. A brief introduction of the adopted model is provided as follows, and a more detailed description can be referred to [30].

The architecture of the employed model is shown in the top of Fig. 2, and the detailed expressions of each branch current are [30]

$$\begin{cases} I_k(t_i) = I_k(0)e^{-\frac{t_i}{\tau_k}} + \dfrac{V_{\mathrm{t}} - V_{\mathrm{OC}}}{R_k}\left(1 - e^{-\frac{t_i}{\tau_k}}\right) \\ \qquad i = 1, 2, \ldots, N \\ \displaystyle\sum_{k=1}^{2} I_k(t_i) = I(t_i) \end{cases} \tag{1}$$

where t_i denotes the CV charging time, $t_1 = 0$ denotes the start of the CV charging process, N denotes the data size,

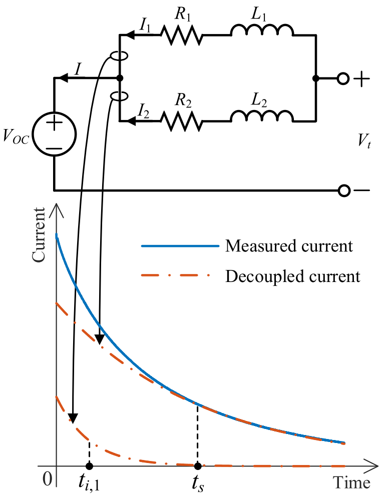

Fig. 2. Schematic representation of employed ECM, CV charging current, and corresponding decoupled currents.

t_{i+1}–t_i denotes the sampling interval (T_s), V_t denotes the battery terminal voltage, V_{OC} denotes the open circuit voltage, I denotes the load current (the positive value and the negative value represent charging and discharging, respectively), $I_k(t_i)$ ($k = 1$ and 2) denotes the branch current through each RL network, R_k, L_k, and τ_k denote the resistance, the inductance, and the time constant for each RL network, respectively, and $\tau_k = L_k/R_k$. Specifically, τ_1 and τ_2 represent the fast-dynamic and slow-dynamic characteristics of the CV charging current, respectively, that is, $\tau_1 < \tau_2$.

It can be observed from (1) that the CV charging current can be decoupled into two parts with different scales of time constants, as schematically shown in Fig. 2. In addition, the $(V_t - V_{OC})(1 - e^{-(t_i/\tau_k)})/R_k$ part in (1) can be negligible because of the relatively low (V_t–V_{oc}) and high R_k [30]. Therewithal, (1) can be simplified as

$$I(t_i) = I_1(t_i) + I_2(t_i) = I_1(0)e^{-\frac{t_i}{\tau_1}} + I_2(0)e^{-\frac{t_i}{\tau_2}} \quad (2)$$

where $I_1(t_i)$ and $I_2(t_i)$ denote the fast-dynamic and the slow-dynamic currents, respectively.

Assuming $I_1(t_i)$ reduces to a negligible value at t_s, as shown in Fig. 2, the measured CV charging current mainly contains $I_2(t_i)$ after t_s, as

$$I(t_i) = I_2(t_i) = I_2(0)e^{-\frac{t_i}{\tau_2}}, \quad t_i \geq t_s. \quad (3)$$

The differential expression of (3) is

$$\frac{I(t_i) - I(t_i - L)}{L} \approx I'(t_i) = -\frac{I_2(0)}{\tau_2}e^{-\frac{t_i}{\tau_2}} = -\frac{I(t_i)}{\tau_2} \quad (4)$$

where L denotes a certain length of the sampling interval.

Based on (4), the time constant of the slow-dynamic current can be obtained by

$$\tau_{2,\text{est}} = -\frac{I(t_{i,2})}{I'(t_{i,2})}, \quad t_{i,2} \geq t_s \quad (5)$$

where $\tau_{2,\text{est}}$ denotes the estimated τ_2.

Then, $I_2(0)$ can be calculated by substituting $\tau_{2,\text{est}}$ into (3), and the estimated fast-dynamic current ($I_{1,\text{est}}$) can be obtained by subtracting the estimated slow-dynamic current ($I_{2,\text{est}}$) from the measured current. Subsequently, the time constant of the fast-dynamic current can be obtained by

$$\tau_{1,\text{est}} = -\frac{t_{i,1}}{\ln[I_{1,\text{est}}(t_{i,1})/I_{1,\text{est}}(0)]}, \quad t_{i,1} < t_s \quad (6)$$

where $\tau_{1,\text{est}}$ denotes the estimated τ_1. In this study, $t_{i,1}$ is determined as the time when the estimated fast-dynamic current decreases to 36.8% of the initial value.

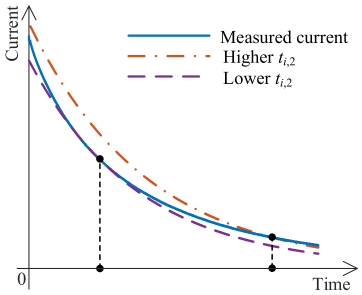

Fig. 3. Example of the slow-dynamic current estimation result: the parameter identification is exemplarily performed based on the data of the NCA battery.

It should be noted from (5) that $\tau_{2,\text{est}}$ is closely related to $t_{i,2}$. When the selected $t_{i,2}$ is far less than t_s, $\tau_{2,\text{est}}$ is generally lower than the actual value, leading to a relatively significant difference between the estimated and the measured currents, especially at the end of the CV charging process, which is exemplarily shown as the dashed line in Fig. 3. In contrast, when the selected $t_{i,2}$ is much larger than t_s, the identified model parameters cannot effectively reflect the fast-dynamic characteristic of the measured current, and $I_{2,\text{est}}$ may above the measured current in the former part of the CV charging process (the dotted-dashed line in Fig. 3), resulting in the negative $I_{1,\text{est}}$, which has no physical meaning. Hence, it is critical to determine an appropriate $t_{i,2}$. In this study, the selected $t_{i,2}$ ($t_{i,2,n}$) is decreased from a predefined value (T_0) at a certain time interval (ΔT), as

$$t_{i,2,n} = T_0 - n\Delta T, \quad T_0 \leq T_{\text{CV}} \text{ and } \Delta T \geq T_s. \quad (7)$$

Then, the unknown model parameters are identified based on the charging data with different $t_{i,2}$s, and the parameters corresponding to the lowest root-mean-square error (RMSE) between the estimated and the measured currents are selected as the final model parameter. The objective function can be expressed as

$$\hat{\theta}_n = \arg\min[\text{RMSE}(\theta_n)] \quad (8)$$

where θ_n denotes the unknown model parameters corresponding to $t_{i,2,n}$, and $\theta_n = [\tau_{1,\text{est},n}, \tau_{2,\text{est},n}, I_{1,\text{est},n}(0), I_{2,\text{est},n}(0)]$. RMSE($\theta_n$) can be further expressed as

$$\text{RMSE}(\theta_n) = \sqrt{\frac{1}{N}\sum_{i=1}^{N}[I_{\text{mea}}(t_i) - I_{\text{est}}(t_i, \theta_n)]^2} \quad (9)$$

where $I_{\text{mea}}(\cdot)$ and $I_{\text{est}}(\cdot)$ denote the measured and the estimated currents, respectively.

The overall parameter identification framework based on the decoupled dynamic characteristic of the CV charging current

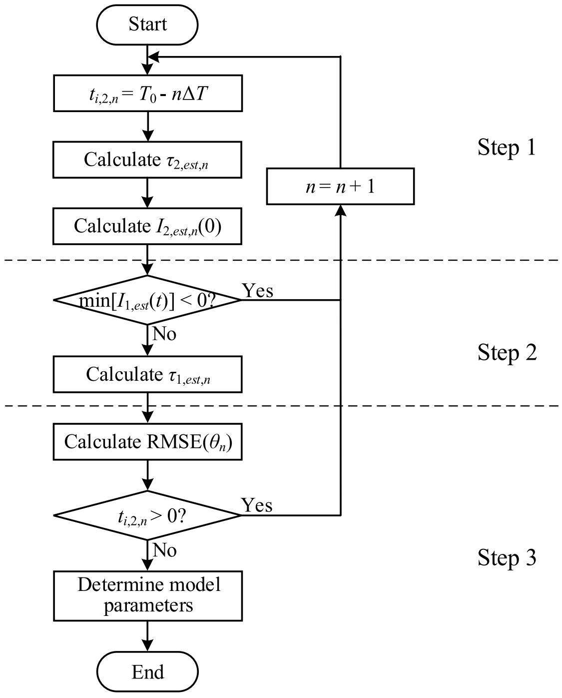

Fig. 4. Proposed parameter identification scheme.

is presented in Fig. 4. The time-current series, denoted as $[t_i, I_{\text{mea}}(t_i)]$, are recorded in the storage component as soon as the charging mode is transformed to the CV phase, and the proposed parameterization method is conducted when the charging process is completed. The proposed parameter identification scheme mainly includes the following three steps.

Step 1: Identifying the slow-dynamic model parameters. First of all, $\tau_{2,\text{est},n}$ is estimated according to (5). Then, $I_{2,\text{est},n}(0)$ is calculated by substituting $\tau_{2,\text{est},n}$ into (3). Afterward, the slow-dynamic current is estimated based on the preliminarily identified model parameters.

Step 2: Identifying the fast-dynamic model parameters. $I_{1,\text{est}}$ is calculated by subtracting $I_{2,\text{est}}$ from I_{mea}. If the minimum value of $I_{1,\text{est}}$ is negative, a new set of slow-dynamic model parameters corresponding to $t_{i,2,n+1}$ should be identified. Otherwise, $\tau_{1,\text{est},n}$ can be obtained according to (6).

Step 3: Determining the model parameters. The RMSE between the estimated and the measured currents is calculated for each $t_{i,2,n}$. The optimal model parameters are determined by searching for the lowest RMSE.

III. FoI SELECTION

As reported, the battery SoH, especially the state of the capacity degradation, can be effectively calculated by the dynamic characteristic of the CV charging current [24]. Consequently, the battery SoH in this study is defined as

$$\text{SoH} = \frac{\text{Cap}_{\text{actual}}}{\text{Cap}_{\text{nominal}}} \times 100\% \tag{10}$$

where $\text{Cap}_{\text{actual}}$ and $\text{Cap}_{\text{nominal}}$ denote the actual battery capacity and the nominal battery capacity, respectively.

Based on the aforementioned parameter identification technique, the dynamic characteristics of the decoupled CV charging currents for the new and aged batteries are investigated in this section, and the effective FoIs are extracted to correlate with the battery capacity loss. Specifically, the CV charging current of the lithium iron phosphate (LFP) and the nickel cobalt aluminum oxide (NCA) batteries are exemplarily employed to make a qualitative analysis.

For the tested LFP battery, the measured charging currents and the corresponding decoupled currents are plotted in Fig. 5(a), (c), and (e), respectively. It can be observed from Fig. 5(a) that the variation rate of the current profile decreases as the battery ages. Similarly, compared to the new state battery, the fast-dynamic and the slow-dynamic currents of the aged state battery need more time to decrease to the steady state, as shown in Fig. 5(c) and (e). For the decoupled current, the corresponding time constant is represented by the intersection of the tangent line of the current curve at the initial point and the time axis. It can be observed from Fig. 5(c) and (e) that for both decoupled currents, the time constants corresponding to the aged battery are generally larger than the time constants of the new battery.

For the NCA battery, the CV charging current, the decoupled fast-dynamic and slow-dynamic parts at new and aged states are demonstrated in Fig. 5(b), (d), and (f), respectively. Represented in Fig. 5(d) and (f), the proportion of the fast-dynamic current to the overall current is negligible for a new battery and increases significantly for an aged battery. In addition, it can be seen from Fig. 5(f) that although the initial value of the slow-dynamic current for the aged battery is lower than the value for the new battery, the slow-dynamic current still requires a longer convergence time, which means a larger time constant for the corresponding current curve, that is, $\tau_{2,\text{aged}} > \tau_{2,\text{new}}$. Based on the above analysis, we can conclude that compared with the new battery, the CV charging current for the aged battery demonstrates a faster rate of decrease in the initial stage. After a certain amount of time, when the influence of the fast-dynamic current can be omitted, the slow-dynamic current dominates the charging current, and the variation rate of the current curve for the aged battery decreases, leading to a longer CV charging time, as shown in Fig. 5(b).

Hence, the time constant of the decoupled current can be considered as the effective FoI to reflect the battery capacity fade, and the actual battery capacity can be estimated according to the evolution of the corresponding time constant.

IV. VALIDATION AND DISCUSSION

A. Experimental Setup and Test Procedure

Two types of batteries are employed in this study, that is, four 2500-mAh 26650 batteries (numbered from #1 to #4) with an LFP-positive electrode, and six 4800-mAh 21700 batteries (numbered from #5 to #10) with NCA cathode material. Specifically, all four LFP batteries were placed in an air-conditioned room (25 ± 2 °C) and were charged/discharged by an eight-channel Arbin BT2000 battery cycler. All NCA batteries were placed in a thermal chamber (GD-4015) at

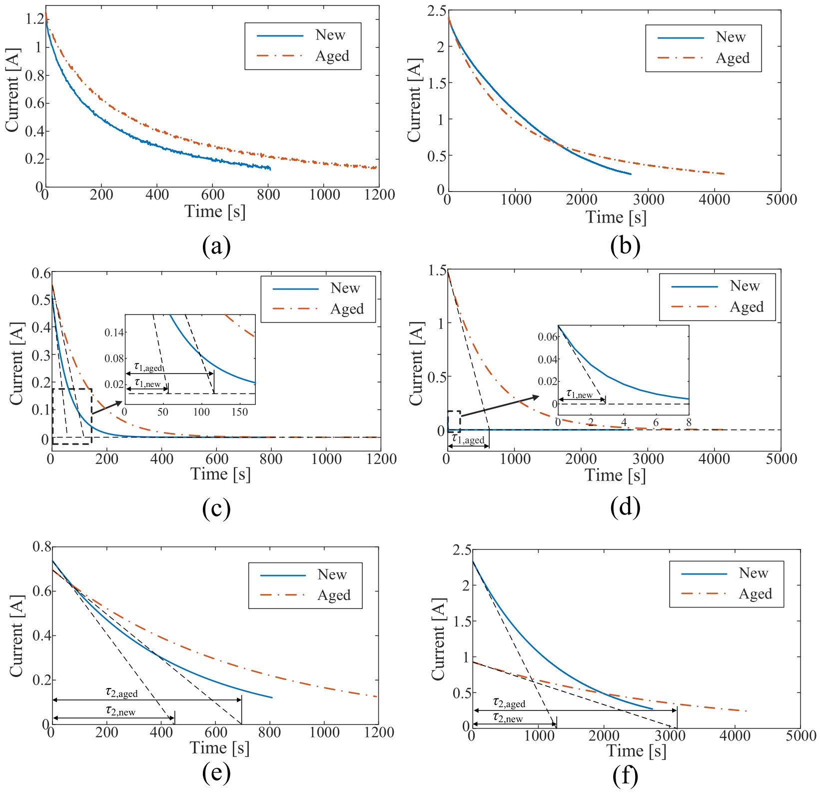

Fig. 5. Representative CV charging currents and decoupled currents at new and aged states. (a) Measured currents of battery #1. (b) Measured currents of battery #5. (c) Fast-dynamic currents of battery #1. (d) Fast-dynamic currents of battery #5. (e) Slow-dynamic currents of battery #1. (f) Slow-dynamic currents of battery #5.

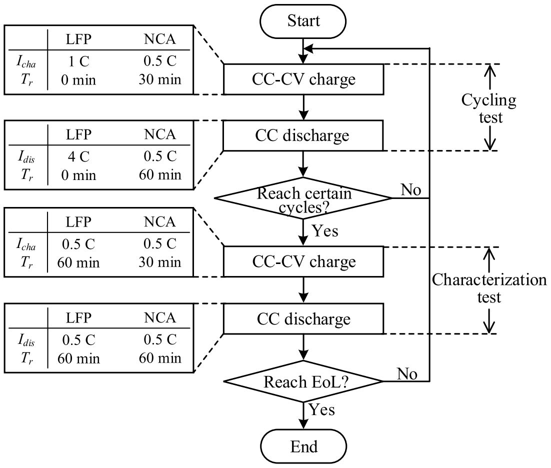

Fig. 6. Battery test procedure.

TABLE I

Benchmark Model Parameters

	t_{sim} [s]	$I_{1,ref}(0)$ [A]	$I_{2,ref}(0)$ [A]	$\tau_{1,ref}$ [s]	$\tau_{2,ref}$ [s]
Case #1	1000	0.55	0.7	80	500
Case #2	2000	1.0	1.4	500	2000

25 °C, and the tests were conducted by a 16-channel NBT5V20AC16-T battery cycler.

In this study, all the tested batteries were cycled under 100% depth of discharge, the cutoff current under the CV charging scenario was 0.05 C for both types of batteries, the CC–CV transition voltages were 3.65 and 4.2 V for the LFP and the NCA batteries, respectively, and the discharge cutoff voltages were 2.0 and 2.5 V for the LFP and the NCA batteries, respectively. The detailed test procedures for the two categories of batteries are shown in Fig. 6, where I_{cha} and I_{dis} denote the C-rates of charging and discharging currents, respectively, and T_r denotes the rest period after the charge/discharge process. The current, battery terminal voltage, temperature, and accumulative capacity were recorded with the sampling rate of 1 Hz during the tests. In this study, the actual battery capacity is the discharged capacity measured from the characterization test, and all the single battery analyses are based on the test data of batteries #1 (LFP) and #5 (NCA) unless otherwise notified.

B. Parameter Identification Performance Analysis

1) Simulation Verification: The simulation study is performed in MATLAB to preliminarily assess the proposed parameter identification method from the theoretical perspective. The detailed simulation and benchmark model parameters are listed in Table I, where t_{sim} represents the simulation time, $I_{1,\text{ref}}(0)$, $I_{2,\text{ref}}(0)$, $\tau_{1,\text{ref}}$, and $\tau_{2,\text{ref}}$ represent the benchmark values of $I_1(0)$, $I_2(0)$, τ_1, and τ_2, respectively. Specifically, the parameters in Case #1 and Case #2 are set to refer to the

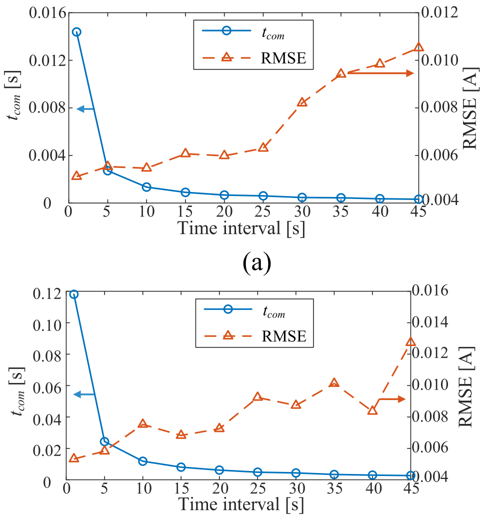

(a)

(b)

Fig. 7. Evolution of RMSE and t_{com} with respect to time interval. (a) Case #1. (b) Case #2.

actual parameters of the employed LFP and NCA batteries, respectively. The random noise with a standard deviation of 5 mA is utilized to simulate the actual measurement noise.

It is evident from (7) that the determination of $t_{i,2,n}$ is closely related to ΔT, thus a parametric study is conducted to investigate the influence of ΔT on the simulation results. Specifically, $t_{i,2,n}$ is decreased at different ΔTs $(1, 5, 10, \ldots, 45)$, and the corresponding simulation results are plotted in Fig. 7. The RMSE between the estimated and benchmark currents is used to measure the parameter identification accuracy and to quantify the computational cost, each identification algorithm is conducted (on a 3-GHz processor and with 16-GB RAM) repeatedly for five times to obtain the average computational time (t_{com}). Generally, the reduced ΔT corresponds to the enhanced resolution of $t_{i,2,n}$, leading to the overall decreasing RMSE and increasing t_{com}, as shown in Fig. 7. Moreover, it should be noted that the identification algorithm implemented in Case #1 presents a higher computational speed than in Case #2, especially with lower ΔT, which can be attributed to the smaller data size. Hence, considering both the identification accuracy and the computational cost, ΔT in Case #1 and Case #2 are set as 1 and 5 s, respectively, for the subsequent simulation study.

To further evaluate the proposed decoupled current-based parameter identification method, the NLS method and the particle swarm optimization (PSO) method, which have been widely utilized in [31], are also conducted to make a comparison in terms of the computational cost and the estimation accuracy. Specifically, the initial condition of the NLS method is set as: $I_0 = I(0)/2$ A, $\tau_1 = 100$ s, $\tau_2 = 1000$ s, the lower and upper bounds of the PSO method are [0 0 0] and [$I(0)/2$ Inf Inf], respectively, and the maximum number of iterations (n_{iter}) is set as 50 in both simulation cases. The comparative results are listed in Table II. As can be seen, the proposed method yields a slightly larger error than the NLS method, while the corresponding computational efficiency is significantly improved, especially compared to the PSO method. It should be noted that the performance of the PSO method is closely dependent on the predefined n_{iter}. The reduced n_{iter} can effectively improve the computational speed, but at the expense of the degrading identification accuracy.

TABLE II
COMPARISON OF SIMULATION RESULTS BASED ON THE CONVENTIONAL AND PROPOSED METHODS

	PSO		**NLS**		**Proposed method**	
	t_{com} **[ms]**	**RMSE [A]**	t_{com} **[ms]**	**RMSE [A]**	t_{com} **[ms]**	**RMSE [A]**
Case #1	480.1	0.0064	47.6	0.0051	14.4	0.0051
Case #2	505.8	0.0061	56.9	0.0050	24.4	0.0058

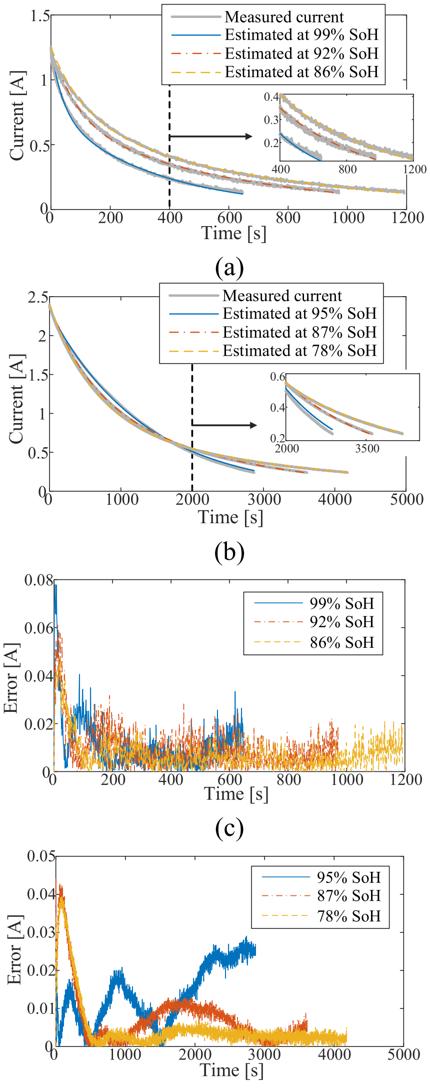

(a)

(b)

(c)

(d)

Fig. 8. Estimation results and absolute values of errors of CV charging current at different aging states. (a) Estimation results for LFP battery. (b) Estimation results for NCA battery. (c) Absolute value of error for LFP battery. (d) Absolute value of error for NCA battery.

2) Experimental Verification: According to the aforementioned discussion, ΔTs for the LFP and the NCA batteries are determined as 1 and 5 s, respectively. Based on the

TABLE III
COMPARISON OF EXPERIMENTAL RESULTS BASED ON THE CONVENTIONAL AND PROPOSED METHODS

Type	SoH	PSO		NLS		Proposed method	
		t_{com} [ms]	RMSE [A]	t_{com} [ms]	RMSE [A]	t_{com} [ms]	RMSE [A]
LFP	99%	496.1	0.0171	86.1	0.0155	29.7	0.0159
	92%	885.5	0.0144	75.7	0.0130	33.0	0.0132
	86%	905.0	0.0122	64.5	0.0102	41.4	0.0102
NCA	95%	500.5	0.0176	183.1	0.0141	46.8	0.0156
	87%	844.3	0.0117	113.3	0.0093	72.9	0.0108
	78%	1010.9	0.0087	118.6	0.0078	66.2	0.0087

employed ΔT, the estimated currents and the corresponding absolute values of errors for both tested batteries at different aging states are plotted in Fig. 8. As can be seen, the estimated currents can generally track the measurements at different aging states, and the absolute values of errors are within 80 and 50 mA for the LFP and the NCA batteries, respectively, suggesting the feasibility and the universality of the proposed parameter identification method.

Besides the proposed method, the NLS and PSO methods are also conducted based on the test data for comparison purposes. Specifically, the initial and boundary conditions of the two conventional methods are consistent with the values set in the simulation study. The comparative results are listed in Table III. Similar to the simulation results, the PSO shows the overall largest t_{com} and RMSE among the utilized three methods. With respect to the NLS method, the lowest t_{com} corresponds to identifying the model parameters for the LFP battery at 86% SoH and the NCA battery at 87% SoH, respectively. This is mostly due to the fact that the predetermined initial values of model parameters are close to the corresponding optimal values, which can reduce the searching time. As observed in Table III, the estimation results of the NCA battery generally present a higher accuracy, that is, the lower values of RMSE, than the results of the LFP battery, especially based on the parameters identified through the NLS method. This phenomenon is supposed to be caused by the inappropriate initial and/or boundary values, as well as the noisy measurements. As can be seen from Fig. 8, the measured current of the LFP battery fluctuates more heavily than the measurements of the NCA battery. It can also be discovered from Table III that, compared to the NLS method, the overall RMSEs of the proposed method are increased by approximately 1.55% and 12.50% for the LFP and the NCA batteries, respectively, but the overall t_{com}s of the proposed method are reduced by approximately 54.0% and 55.2% for the LFP and the NCA batteries, respectively. Hence, it can be concluded that the proposed method demonstrates the reduced computational cost with satisfactory parameter identification accuracy, which is consistent with the simulation results.

C. Correlation Analysis

The relationship between the time constant and the capacity for battery #1 (LFP) and #5 (NCA) is demonstrated in Fig. 9.

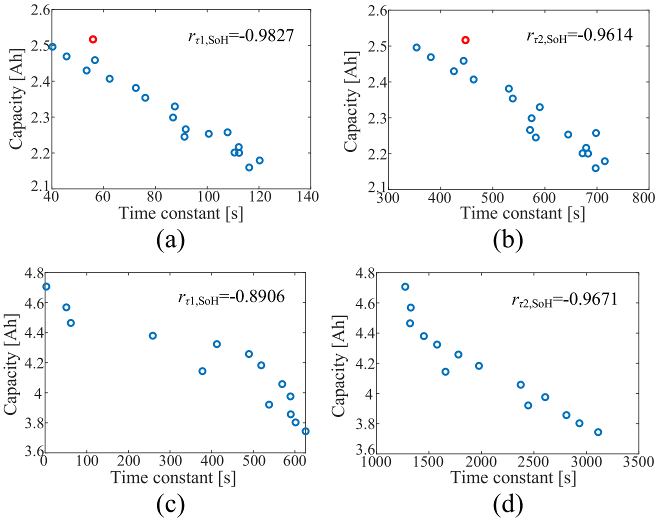

Fig. 9. Evolution of capacity with respect to the time constant of decoupled current. (a) τ_1 for battery #1. (b) τ_2 for battery #1. (c) τ_1 for battery #5. (d) τ_2 for battery #5.

It can be observed that the overall battery capacity decreases with the increasing time constant.

For the employed LFP battery, the battery capacity decreases linearly with respect to the time constants of two decoupled currents, as shown in Fig. 9(a) and (b). It should be noted that the data points corresponding to the new battery are deviated from the trend lines, as marked by the red circles in Fig. 9(a) and (b), which may be attributed to the inactive electrode at the beginning stage of life. The Pearson product–moment correlation coefficients ($r_{x,y}$) are displayed in Fig. 9(a) and (b) to quantify the correlation between the battery capacity and the time constant. $r_{x,y}$ can be calculated by

$$r_{x,y} = \frac{\sum_{i=1}^{N}(x_i-\bar{x})(y_i-\bar{y})}{\sqrt{\sum_{i=1}^{N}(x_i-\bar{x})^2}\sqrt{\sum_{i=1}^{N}(y_i-\bar{y})^2}} \tag{11}$$

where x and y represent the selected time constant and the battery capacity, respectively, and $\bar{x}$ and $\bar{y}$ denote mean values of x and y, respectively. Specifically, the data corresponding to the new battery are not considered in this study.

The correlation coefficients in Fig. 9(a) and (b) indicate that the time constants of two decoupled currents have a negative correlation with the battery capacity. Furthermore, compared to τ_2, τ_1 demonstrates a stronger correlation with the battery capacity. Consequently, τ_1 is selected as the FoI for the tested LFP batteries, and the linear regression function, expressed as (12), is adopted to characterize the correlation according to the variation trend, where Cap_{est} denotes the estimated battery capacity. Specifically, the normalized FoIs are used to reduce the influence of the battery inconsistency on the SoH estimation [32]. The RMSE of the capacity estimation is 0.0193 Ah, that is, 0.77% of the nominal capacity, indicating the feasibility of the fit correlation

$$\text{Cap}_{\text{est}} = -0.1653\tau_{1,\text{est}} + 2.6638. \tag{12}$$

For the tested NCA battery, nonlinear relationships between the battery capacity and the time constants are presented

TABLE IV
ESTIMATION ERROR OF (13)

		$\tau_{2,est} \leq 1.094$	$\tau_{2,est} > 1.094$	**Overall**
RMSE	[Ah]	0.0650	0.0507	0.0541
	[%]	1.35%	1.06%	1.13%

in Fig. 9(c) and (d). It can be observed that τ_2 presents a significantly stronger correlation with the battery capacity, in comparison to τ_1. Specifically, two stages of the variation trend can be distinguished for the capacity degradation as a function of τ_2: 1) a faster capacity degradation rate at the beginning of life and 2) a slowly and linearly decreasing trend afterward. Hence, the above correlation can be mathematically expressed as

$$\begin{cases} \mathrm{Cap}_{\mathrm{est}} = 8.6383\tau_{2,\mathrm{est}}^2 - 18.9011\tau_{2,\mathrm{est}} + 14.7192 \\ \qquad \tau_{2,\mathrm{est}} \leq 1.094 \\ \mathrm{Cap}_{\mathrm{est}} = -0.4739\tau_{2,\mathrm{est}} + 4.8617 \\ \qquad \tau_{2,\mathrm{est}} > 1.094. \end{cases} \tag{13}$$

The RMSEs computed based on the test data of battery #5 are summarized in Table IV to preliminarily evaluate the fitting performance of (13). As can be seen, the fit regression function can estimate the battery capacity with an acceptable overall RMSE of 0.0541 Ah. Besides, the estimation error calculated when $\tau_{2,\mathrm{est}} \leq 1.094$ is larger than the error when $\tau_{2,\mathrm{est}} > 1.094$, which may be attributed to the lack of fitting samples in the first stage.

D. SoH Estimation Performance Analysis

Based on the aforementioned discussion, τ_1 and τ_2 are selected as FoIs for the tested LFP and the NCA batteries, respectively. To investigate the influence of the parameter identification on the subsequent SoH estimation, the proposed parameter identification and the NLS methods are both performed to extract the decoupled time constants. Furthermore, T_{CV} and the coefficient B of the empirical function, as two other commonly used FoIs based on the CV charging data, are also adopted to make a comparison [18], [21].

The evolutions of the capacity with respect to the normalized τ_{1_pro}, τ_{1_NLS}, T_{CV}, and $1/B$ for four LFP batteries are plotted in Fig. 10, where τ_{k_pro} and τ_{k_NLS} ($k = 1$ or 2) in this study denote the decoupled time constant identified through and the proposed and the NLS methods, respectively. Specifically, the reciprocal of B ($1/B$) is employed to make a comparison since it can be considered as the time constant of the CV charging current curve. The solid lines in Fig. 10 represent the reference regression functions based on the test data of battery #1, which can be expressed as (12), (14), (15), and (16), respectively,

$$\mathrm{Cap}_{\mathrm{est}} = -0.1627\tau_{1\_\mathrm{NLS}} + 2.6670 \tag{14}$$

$$\mathrm{Cap}_{\mathrm{est}} = -0.3596T_{\mathrm{CV}} + 2.8693 \tag{15}$$

$$\mathrm{Cap}_{\mathrm{est}} = -0.3873(1/B) + 2.8958. \tag{16}$$

In addition, the detailed RMSEs of the estimated capacities and SoHs are listed in Table IV for the quantitative evaluation.

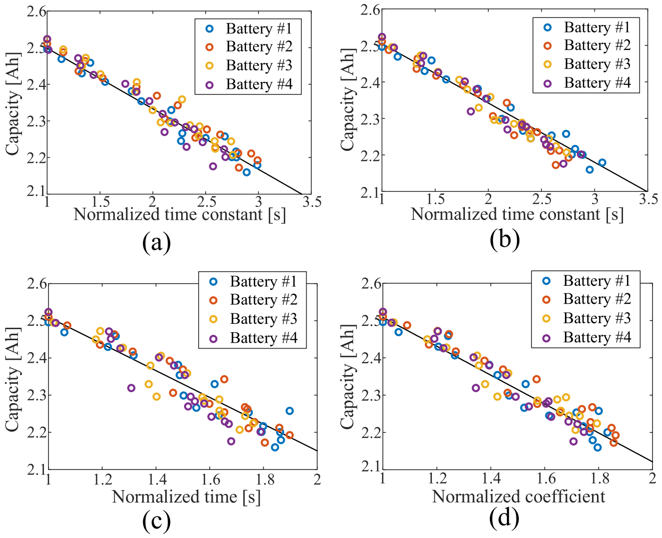

Fig. 10. Evolutions of capacity with respect to different FoIs for four LFP batteries. (a) τ_{1_pro}. (b) τ_{1_NLS}. (c) T_{CV}. (d) $1/B$.

TABLE V
RMSES OF ESTIMATION RESULTS FOR FOUR LFP BATTERIES BY DIFFERENT FOIS

Number	τ_{1_pro}		τ_{1_NLS}		T_{CV}		$1/B$	
	[Ah]	[%]	[Ah]	[%]	[Ah]	[%]	[Ah]	[%]
#1	0.0194	0.78%	0.0193	0.77%	0.0325	1.30%	0.0274	1.10%
#2	0.0249	1.00%	0.0266	1.06%	0.0305	1.22%	0.0292	1.17%
#3	0.0269	1.08%	0.0202	0.81%	0.0300	1.20%	0.0262	1.05%
#4	0.0254	1.02%	0.0251	1.00%	0.0427	1.71%	0.0270	1.08%
Mean	0.0241	0.97%	0.0228	0.91%	0.0339	1.36%	0.0274	1.10%

It can be observed that the overall results from the LFP battery show satisfactory estimation accuracy (the mean RMSEs of all the SoH estimation results are within 1.5%). It can be observed from Fig. 10 and Table V that the actual battery capacity estimated based on τ_{1_NLS} demonstrates a slightly superior accuracy compared to the estimation based on τ_{1_pro}, which is supposed to be brought by the more precise parameter identification as discussed in Section IV-B. Moreover, compared with the mean RMSEs corresponding to T_{CV} and $1/B$, the mean RMSE corresponding to τ_{1_pro} is reduced by approximately 28.7% and 11.8%, respectively, suggesting the feasibility of the developed reference correlation.

Six groups of NCA battery aging data are adopted to further validate the universality of the proposed method. The actual capacities of all six batteries are plotted as functions of τ_{2_pro}, τ_{2_NLS}, T_{CV}, and $1/B$ in Fig. 11(a)–(d), respectively. In Fig. 11(a)–(d), battery #5 is considered as the reference battery, and the reference correlations are mathematically expressed as (13), (17), (18), and (19), respectively,

$$\begin{cases} \mathrm{Cap}_{\mathrm{est}} = 16.6334\tau_{2\_\mathrm{NLS}}^2 - 36.8128\tau_{2\_\mathrm{NLS}} + 24.7485 \\ \qquad \tau_{2\_\mathrm{NLS}} \leq 1.107 \\ \mathrm{Cap}_{\mathrm{est}} = -0.5287\tau_{2\_\mathrm{NLS}} + 4.9349 \\ \qquad \tau_{2\_\mathrm{NLS}} > 1.107 \end{cases} \tag{17}$$

$$\mathrm{Cap}_{\mathrm{est}} = -1.7782T_{\mathrm{CV}} + 6.3396 \tag{18}$$

$$\mathrm{Cap}_{\mathrm{est}} = -7.2032(1/B)^2 + 15.0887(1/B) - 3.3522. \tag{19}$$

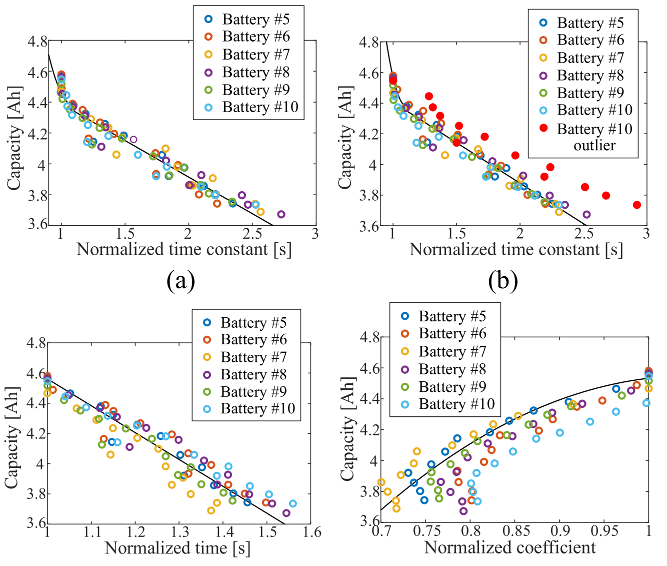

(a) (b) (c) (d)

Fig. 11. Evolutions of capacity with respect to different FoIs for six NCA batteries. (a) τ_{2_pro}. (b) τ_{2_NLS}. (c) T_{CV}. (d) $1/B$.

TABLE VI

RMSES OF ESTIMATION RESULTS FOR SIX NCA BATTERIES BY DIFFERENT FOIS

Number	τ_{2_pro}		τ_{2_NLS}		T_{CV}		$1/B$	
	[Ah]	**[%]**	**[Ah]**	**[%]**	**[Ah]**	**[%]**	**[Ah]**	**[%]**
#5	0.0541	1.13%	0.0458	0.95%	0.0608	1.27%	0.0668	1.39%
#6	0.0654	1.36%	0.0530	1.10%	0.0829	1.73%	0.1732	3.61%
#7	0.0870	1.81%	0.1028	2.14%	0.1357	2.83%	0.0985	2.05%
#8	0.0628	1.31%	0.0537	1.12%	0.0748	1.56%	0.1775	3.70%
#9	0.0496	1.03%	0.0676	1.41%	0.0813	1.69%	0.0936	1.95%
#10	0.0641	1.34%	0.0675	1.41%	0.0989	2.06%	0.2252	4.69%
Mean	0.0638	1.33%	0.0651	1.36%	0.0891	1.86%	0.1391	2.90%

It should be noted from Fig. 11(b) that unlike the results of the LFP battery, the estimated capacity of battery #10 cannot track the reference values, which are marked as the red dots. By comparison, the estimation performance is significantly improved when the initial condition of battery #10 is reset as: $I_0 = I(0)/2$ A, $\tau_1 = 500$ s, $\tau_2 = 2000$ s, where the light blue circles in Fig. 11(b) represent the corresponding reference capacity. This indicates the sensitivity of the SoH estimation to the predefined initial condition when the FoI is identified by the NLS method. In addition, it can be concluded from Fig. 11 that the capacities estimated by the τ_{2_pro}-based reference correlation yields a similar variation trend of the actual capacities for all six batteries, demonstrating the best performance among the three FoIs. By contrast, there exists obvious deviations between the actual and the estimated capacities based on the coefficient $1/B$, especially when $1/B$ is approximately lower than 0.8. Furthermore, the corresponding RMSEs of the estimation results are summarized in Table VI. Specifically, the estimation error corresponding to τ_{2_NLS} of battery #10 is based on the modified initial condition. It can be observed that the capacities estimated based on τ_{2_pro} yield the lowest RMSEs (the mean RMSEs are reduced by approximately 28.5% and 54.1%), in comparison with the results based on T_{CV} and $1/B$, indicating the superiority of the proposed method.

V. CONCLUSION

A novel SoH estimation method based on the decoupled dynamic characteristic of the CV charging current is developed in this study. Two types of batteries are adopted under multiple tests to validate the feasibility and the universality of the proposed method. According to the simplified second-order *RL* network-based ECM, a parameter identification method is proposed based on the decoupled current behavior. Compared with the conventional NLS method, the proposed dynamic-decoupled method demonstrates a lower computational burden and satisfactory identification accuracy. Based on the correlation analysis, τ_1 and τ_2 are selected as FoIs for the tested LFP and NCA batteries, respectively. The corresponding RMSEs of the estimation results by the reference correlation are within 0.0269 (1.08% of the nominal capacity) and 0.0870 Ah (1.81% of the nominal capacity) for the two employed batteries. Furthermore, the selected FoI demonstrates the best SoH estimation performance in comparison to T_{CV}, and $1/B$, as two other widely used FoIs extracted from the CV charging data.

It is worth noting that although the normalized FoIs have been utilized to reduce the influence of the battery inconsistency on the SoH estimation, there still exists obvious differences between the estimated and the actual battery capacity, such as the estimation results for battery #7. This limits the applicability of the reference correlation. Hence, a more effective inconsistency reduction technique will be explored in future work to improve the universality of the proposed method.

REFERENCES

[1] X. Zhang and C. Mi, *Vehicle Power Management: Modeling, Control and Optimization*. Berlin, Germany: Springer, 2011.

[2] Z. Deng, X. Hu, X. Lin, L. Xu, J. Li, and W. Guo, "A reduced-order electrochemical model for all-solid-state batteries," *IEEE Trans. Transport. Electrific.*, vol. 7, no. 2, pp. 464–473, Jun. 2021.

[3] Z. Wei, J. Zhao, H. He, G. Ding, H. Cui, and L. Liu, "Future smart battery and management: Advanced sensing from external to embedded multi-dimensional measurement," *J. Power Sources*, vol. 489, Mar. 2021, Art. no. 229462.

[4] S. Yang, C. Zhang, J. Jiang, W. Zhang, L. Zhang, and Y. Wang, "Review on state-of-health of lithium-ion batteries: Characterizations, estimations and applications," *J. Cleaner Prod.*, vol. 314, Sep. 2021, Art. no. 128015.

[5] Y. Gao, K. Liu, C. Zhu, X. Zhang, and D. Zhang, "Co-estimation of state-of-charge and state-of-health for lithium-ion batteries using an enhanced electrochemical model," *IEEE Trans. Ind. Electron.*, early access, Mar. 23, 2021, doi: 10.1109/TIE.2021.3066946.

[6] R. Xiong, L. Li, and J. Tian, "Towards a smarter battery management system: A critical review on battery state of health monitoring methods," *J. Power Sources*, vol. 405, pp. 18–29, Nov. 2018.

[7] A. Tomaszewska *et al.*, "Lithium-ion battery fast charging: A review," *ETransportation*, vol. 1, Aug. 2019, Art. no. 100011.

[8] U. R. Koleti, C. Zhang, R. Malik, T. Q. Dinh, and J. Marco, "The development of optimal charging strategies for lithium-ion batteries to prevent the onset of lithium plating at low ambient temperatures," *J. Energy Storage*, vol. 24, Aug. 2019, Art. no. 100798.

[9] Z. Wei, Z. Quan, J. Wu, Y. Li, J. Pou, and H. Zhong, "Deep deterministic policy gradient-DRL enabled multiphysics-constrained fast charging of lithium-ion battery," *IEEE Trans. Ind. Electron.*, early access, Apr. 7, 2021, doi: 10.1109/TIE.2021.3070514.

[10] D.-I. Stroe and E. Schaltz, "Lithium-ion battery state-of-health estimation using the incremental capacity analysis technique," *IEEE Trans. Ind. Appl.*, vol. 56, no. 1, pp. 678–685, Jan. 2020.

[11] B. Ospina Agudelo, W. Zamboni, and E. Monmasson, "Application domain extension of incremental capacity-based battery SoH indicators," *Energy*, vol. 234, Nov. 2021, Art. no. 121224.

[12] X. Bian, Z. Wei, J. He, F. Yan, and L. Liu, "A novel model-based voltage construction method for robust State-of-Health estimation of lithium-ion batteries," *IEEE Trans. Ind. Electron.*, vol. 68, no. 12, pp. 12173–12184, Dec. 2021.

[13] Y. Li, M. A. Monem, R. Gopalakrishnan, M. Berecibar, E. N. Maury, N. Omar, P. Bossche, and J. V. Mierlo, "A quick on-line state of health estimation method for Li-ion battery with incremental capacity curves processed by Gaussian filter," *J. Power Sources*, vol. 373, pp. 40–53, Jan. 2018.

[14] B. Jiang, H. Dai, and X. Wei, "Incremental capacity analysis based adaptive capacity estimation for lithium-ion battery considering charging condition," *Appl. Energy*, vol. 269, Jul. 2020, Art. no. 115074.

[15] G. Ning, R. E. White, and B. N. Popov, "A generalized cycle life model of rechargeable Li-ion batteries," *Electrochim. Acta*, vol. 51, no. 10, pp. 2012–2022, 2006.

[16] H. Wang, S. Frisco, E. Gottlieb, R. Yuan, and J. F. Whitacre, "Capacity degradation in commercial Li-ion cells: The effects of charge protocol and temperature," *J. Power Sources*, vol. 426, pp. 67–73, Jun. 2019.

[17] R. Mathieu, O. Briat, P. Gyan, and J.-M. Vinassa, "Comparison of the impact of fast charging on the cycle life of three lithium-ion cells under several parameters of charge protocol and temperatures," *Appl. Energy*, vol. 283, Feb. 2021, Art. no. 116344.

[18] N. Williard, W. He, M. Osterman, and M. Pecht, "Comparative analysis of features for determining state of health in lithium-ion batteries," *Int. J. Prognostics Health Manage.*, vol. 4, no. 1, p. 10, Oct. 2020.

[19] D. Yang, X. Zhang, R. Pan, Y. Wang, and Z. Chen, "A novel Gaussian process regression model for state-of-health estimation of lithium-ion battery using charging curve," *J. Power Sources*, vol. 384, pp. 387–395, Apr. 2018.

[20] H. Liu *et al.*, "An analytical model for the CC-CV charge of Li-ion batteries with application to degradation analysis," *J. Energy Storage*, vol. 29, Jun. 2020, Art. no. 101342.

[21] A. Eddahech, O. Briat, and J.-M. Vinassa, "Determination of lithium-ion battery state-of-health based on constant-voltage charge phase," *J. Power Sources*, vol. 258, pp. 218–227, Jul. 2014.

[22] H. Ruan, H. He, Z. Wei, Z. Quan, and Y. Li, "State of health estimation of lithium-ion battery based on constant-voltage charging reconstruction," *IEEE J. Emerg. Sel. Topics Power Electron.*, early access, Jul. 21, 2021, doi: 10.1109/JESTPE.2021.3098836.

[23] Z. Wang, S. Zeng, J. Guo, and T. Qin, "State of health estimation of lithium-ion batteries based on the constant voltage charging curve," *Energy*, vol. 167, pp. 661–669, Jan. 2019.

[24] J. Yang, B. Xia, W. Huang, Y. Fu, and C. Mi, "Online state-of-health estimation for lithium-ion batteries using constant-voltage charging current analysis," *Appl. Energy*, vol. 212, pp. 1589–1600, Feb. 2018.

[25] N. N. Dingari, M. Mynam, and B. Rai, "A reduced-order electrochemical model for coupled prediction of state of charge and state of health of lithium ion batteries under constant current-constant voltage charging conditions," *Energy Storage*, vol. 2, no. 6, p. e194, Dec. 2020.

[26] W. Waag and D. U. Sauer, "Adaptive estimation of the electromotive force of the lithium-ion battery after current interruption for an accurate state-of-charge and capacity determination," *Appl. Energy*, vol. 111, no. 4, pp. 416–427, Nov. 2013.

[27] M. Bruch, L. Millet, J. Kowal, and M. Vetter, "Novel method for the parameterization of a reliable equivalent circuit model for the precise simulation of a battery cell's electric behavior," *J. Power Sources*, vol. 490, Apr. 2021, Art. no. 229513.

[28] A. Hentunen, T. Lehmuspelto, and J. Suomela, "Time-domain parameter extraction method for Thévenin-equivalent circuit battery models," *IEEE Trans. Energy Convers.*, vol. 29, no. 3, pp. 558–566, Sep. 2014.

[29] B. Xia, X. Zhao, R. de Callafon, H. Garnier, T. Nguyen, and C. Mi, "Accurate lithium-ion battery parameter estimation with continuous-time system identification methods," *Appl. Energy*, vol. 179, pp. 426–436, Oct. 2016.

[30] J. Yang, Y. Cai, C. Pan, and C. Mi, "A novel resistor-inductor network-based equivalent circuit model of lithium-ion batteries under constant-voltage charging condition," *Appl. Energy*, vol. 254, Nov. 2019, Art. no. 113726.

[31] X. Lai, W. Gao, Y. Zheng, M. Ouyang, J. Li, X. Han, and L. Zhou, "A comparative study of global optimization methods for parameter identification of different equivalent circuit models for Li-ion batteries," *Electrochim. Acta*, vol. 295, pp. 1057–1066, Feb. 2019.

[32] J. Tian, R. Xiong, and W. Shen, "State-of-Health estimation based on differential temperature for lithium ion batteries," *IEEE Trans. Power Electron.*, vol. 35, no. 10, pp. 10363–10373, Oct. 2020.

Jufeng Yang (Member, IEEE) received the B.S. and Ph.D. degrees in electrical engineering from the Nanjing University of Aeronautics and Astronautics, Nanjing, China, in 2012 and 2019, respectively.

From September 2015 to October 2017, he conducted scientific research as a Joint Ph.D. Student with the Department of Electrical and Computer Engineering, San Diego State University, San Diego, CA, USA. In 2019, he joined the Automotive Engineering Research Institute, Jiangsu University, Zhenjiang, China, as a Faculty Member, where he is currently a Lecturer. His research interests focus on battery management systems, including battery modeling, battery model parameter identification, and battery state estimation.

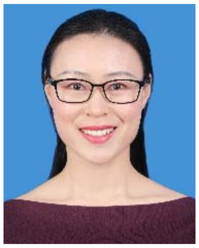

Yingfeng Cai (Senior Member, IEEE) received the B.S., M.S., and Ph.D. degrees from the School of Instrument Science and Engineering, Southeast University, Nanjing, China, in 2006, 2009, and 2013, respectively.

In 2013, she joined the Automotive Engineering Research Institute, Jiangsu University, Zhenjiang, China, where she is currently working as a Professor. Her research interests include computer vision, intelligent transportation systems, intelligent automobiles, and electric vehicles.

Chunting Chris Mi (Fellow, IEEE) received the B.S.E.E. and M.S.E.E. degrees in electrical engineering from Northwestern Polytechnical University, Xi'an, China, in 1985 and 1988, respectively, and the Ph.D. degree in electrical engineering from the University of Toronto, Toronto, ON, Canada, in 2001.

He was with General Electric Company, Peterborough, ON, from 2000 to 2001. He was a Faculty Member with the University of Michigan–Dearborn, Dearborn, MI, USA, from 2001 to 2015. He is currently a Professor of Electrical and Computer Engineering with San Diego State University, San Diego, CA, USA. His research interests include electric drives, power electronics, electric machines, renewable-energy systems, electrical and hybrid vehicles, battery management systems, and wireless power transfer.

Dr. Mi is a fellow of SAE. He was a recipient of Distinguished Teaching Award and Distinguished Research Award from the University of Michigan–Dearborn, 2007 IEEE Region 4 Outstanding Engineer Award, IEEE Southeastern Michigan Section Outstanding Professional Award, SAE Environmental Excellence in Transportation (E2T) Award, IEEE TRANSACTIONS ON POWER ELECTRONICS best paper awards, Prize Letter Award, and the IEEE Power Electronics Emerging Technology Award. He was the Chair from 2008 to 2009 and the Vice-Chair from 2006 to 2007 of the IEEE Southeastern Michigan Section. He was an Area Editor of the IEEE TRANSACTIONS ON VEHICULAR TECHNOLOGY and an Associate Editor of IEEE TRANSACTIONS ON POWER ELECTRONICS and the IEEE TRANSACTIONS ON INDUSTRY APPLICATIONS. He is a Guest Editor of the recent special of the PROCEEDINGS OF THE IEEE.